Chemical and Genetic Engineering of Selective Ion Channel–Ligand Interactions

Christopher J. Magnus,* Peter H. Lee,* Deniz Atasoy,* Helen H. Su, Loren L. Looger, Scott M. Sternson†

Ionic flux mediates essential physiological and behavioral functions in defined cell populations. Cell type–specific activators of diverse ionic conductances are needed for probing these effects. We combined chemistry and protein engineering to enable the systematic creation of a toolbox of ligand-gated ion channels (LGICs) with orthogonal pharmacologic selectivity and divergent functional properties. The LGICs and their small-molecule effectors were able to activate a range of ionic conductances in genetically specified cell types. LGICs constructed for neuronal perturbation could be used to selectively manipulate neuron activity in mammalian brains in vivo. The diversity of ion channel tools accessible from this approach will be useful for examining the relationship between neuronal activity and animal behavior, as well as for cell biological and physiological applications requiring chemical control of ion conductance.

Ion channels are complex molecular machines with critical cell biological functions. Ligand-gated ion channels (LGICs) provide rapid, remote control over conductances for different ions. In neurons, LGICs can be exploited for stimulation or silencing to examine causal relationships between electrical activity and animal behavior.

Several neuron manipulation tools have been derived from LGICs and G protein–coupled receptors (*1*–*4*) that can be genetically targeted and are reported to be orthogonal to endogenous systems. These tools are useful (*5*–*7*) but also face limitations such as ligand instability and lack of brain access (*2*), slow pharmacokinetics (*6*), the need to knock out endogenous alleles (*3*), or reliance on complex intracellular signaling pathways (*4*). Optogenetic tools (*8*–*10*) activate conductances with millisecond precision, but optimization of ion conductance properties has been limited and light targeting is invasive.

To overcome these limitations, we have developed a strategy to create chimeric LGICs with distinct conductance properties derived from modular combinations of pharmacologically selective ligand-binding domains (LBDs) and functionally diverse ion pore domains (IPDs). Within the Cys-loop receptor superfamily, the LBD of the α7 nicotinic acetylcholine receptor (nAChR) behaves as an independent actuator module that can be transplanted onto the IPDs of other Cys-loop receptors (*11*, *12*). These include at least 43 ion channel subunits in vertebrates (*13*), as well as many additional invertebrate (*14*) and prokaryotic (*15*) subunits. Distinct IPDs confer selectivity for chloride or calcium as well as nonspecific cations. For example, splicing the α7 nAChR LBD to the IPDs of the serotonin receptor 3a or the glycine receptor produces chimeric channels (α7-5HT3 or α7-GlyR) with α7 nAChR pharmacology and cation or chloride conductance properties, respectively (*11*, *12*). This modular property is a strong foundation for tailoring functional characteristics. However, the major challenge for using these ion channel LBDs and their ligands as genetically targeted, cell type–selective perturbation tools is that they are already found in the brain; thus, small-molecule agonists will perturb electrical activity in untargeted cell populations. We addressed this challenge by developing an approach to modify the ligand recognition properties of the α7 nAChR LBD using a "bump-hole" strategy (Fig. 1A) (*16*–*18*).

α7 nAChRs are homopentameric channels that form ligand-binding sites at protein-protein interfaces (*19*)—typically a difficult environment for designing small-molecule interactions. We required ion channel activation following ligand binding, which necessitated that molecular alterations be compatible with the operation of these complex molecular machines. Thus, our strategy differed from previous efforts to devise "pharmacological alleles," which used structure-based design to accommodate rigid purine-based antagonists or cofactors into well-defined binding sites in enzymes (*17*, *18*) or small molecule–binding proteins (*16*). To address the additional challenges of pharmacologically engineering ion channels, we used structural models to predict molecular interactions and compensated for uncertainty in these models with functional assays to screen libraries of molecules and mutant ion channels for agonist activity.

First, we modeled the small molecule–protein interaction by homology to the x-ray crystal structure of the snail acetylcholine (ACh) binding protein (*19*) complexed to nicotine (Fig. 1, B and C). We selected the quinuclidinyl benzamide

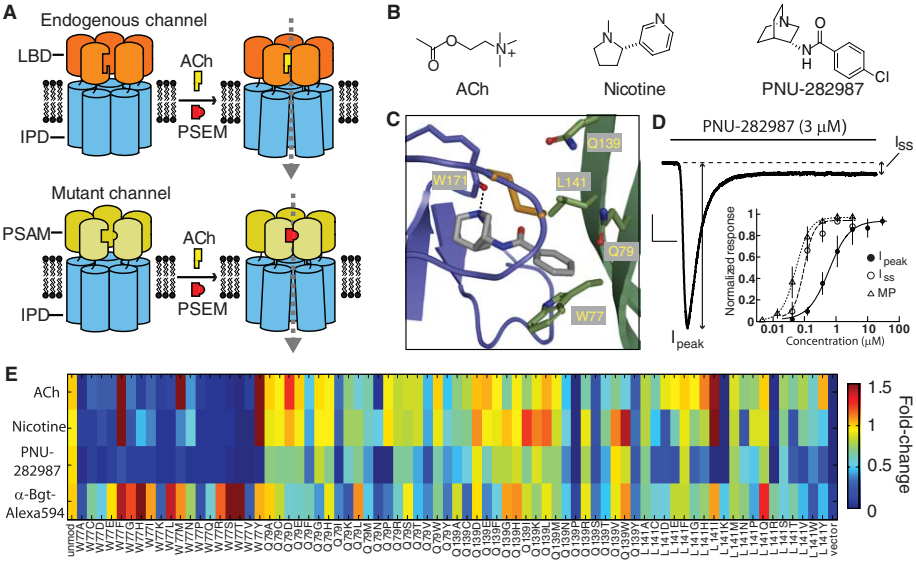

Fig. 1. "Bump-hole" approach to engineering selective ion channel–ligand interactions. (**A**) LGICs composed of ligand binding domain (LBD) and ion pore domain (IPD) modules. LBD mutations yield a pharmacologically selective actuator module (PSAM) that selectively binds pharmacologically selective effector molecules (PSEMs, red) but not the endogenous ligand, ACh (yellow). PSEMs do not bind the unmodified LBD. (**B**) Chemical structures of ACh, nicotine, and PNU-282987. (**C**) Homology model of the α7 nAChR LBD with a docked agonist at the interface between two protomers (purple and green). Residues W77, Q79, Q139, and L141 were targeted for mutagenesis. (**D**) Current evoked by PNU-282987 application to an HEK 293 cell expressing α7-5HT3. A large peak current (I_{peak}) rapidly decays to a persistent, steady-state current (I_{ss}). Black line indicates time course of ligand application. Scale bars: 200 pA, 0.5 s. Inset, Dose response curves (normalized to maximum response) from MP assay correspond to I_{ss} ($n = 3$). Error bars are SEM. (**E**) Color map showing activity and cell surface expression of mutated α7-5HT3 channels. Responses to ACh (100 μM), nicotine (100 μM), PNU-282987 (10 μM), and binding of α-bungarotoxin (Bgt)–Alexa594 were normalized to the response of the unmodified channel to ACh (100 μM) or α-Bgt–Alexa594 binding. Amino acid abbreviations: A, Ala; C, Cys; D, Asp; E, Glu; F, Phe; G, Gly; H, His; I, Ile; K, Lys; L, Leu; M, Met; N, Asn; P, Pro; Q, Gln; R, Arg; S, Ser; T, Thr; V, Val; W, Trp; Y, Tyr.

Janelia Farm Research Campus, Howard Hughes Medical Institute, 19700 Helix Drive, Ashburn, VA 20147, USA.

*These authors contributed equally to this work.
†To whom correspondence should be addressed. E-mail: sternsons@janelia.hhmi.org

PNU-282987 (Fig. 1B), as the starting point for ligand design because it was reported to cross the blood-brain barrier (*20*) and to be highly selective for α7 nAChR (*21*).

(*R*)-3-aminoquinuclidine benzamide, a PNU-282987 analog, was docked with a binding mode analogous to that of nicotine, where the protonated tertiary amine interacts with Trp^{171} and the benzamide interacts primarily with residues on the complementary face of the adjacent protomer (Fig. 1C). Because bulky benzamide substituents were detrimental to activity at the endogenous receptor (*21*), we mutated amino acids proximal to this group—Trp^{77}, Gln^{79}, Gln^{139}, and Leu^{141} (Fig. 1C and fig. S1)—to 19 alternative amino acids each, for a total of 76 mutant channels. Mutant α7 nAChR LBDs were spliced to the IPD of the 5HT3a receptor (fig. S1) and prescreened for cell surface expression and channel activation. Whole-cell voltage clamp recordings of α7-5HT3 responses to PNU-282987 in transfected human embryonic kidney (HEK) 293 cells showed an initial peak current (I_{peak}), which desensitized ($t_{1/2}$ = 0.26 ± 0.07 s, mean ± SD) to a steady-state

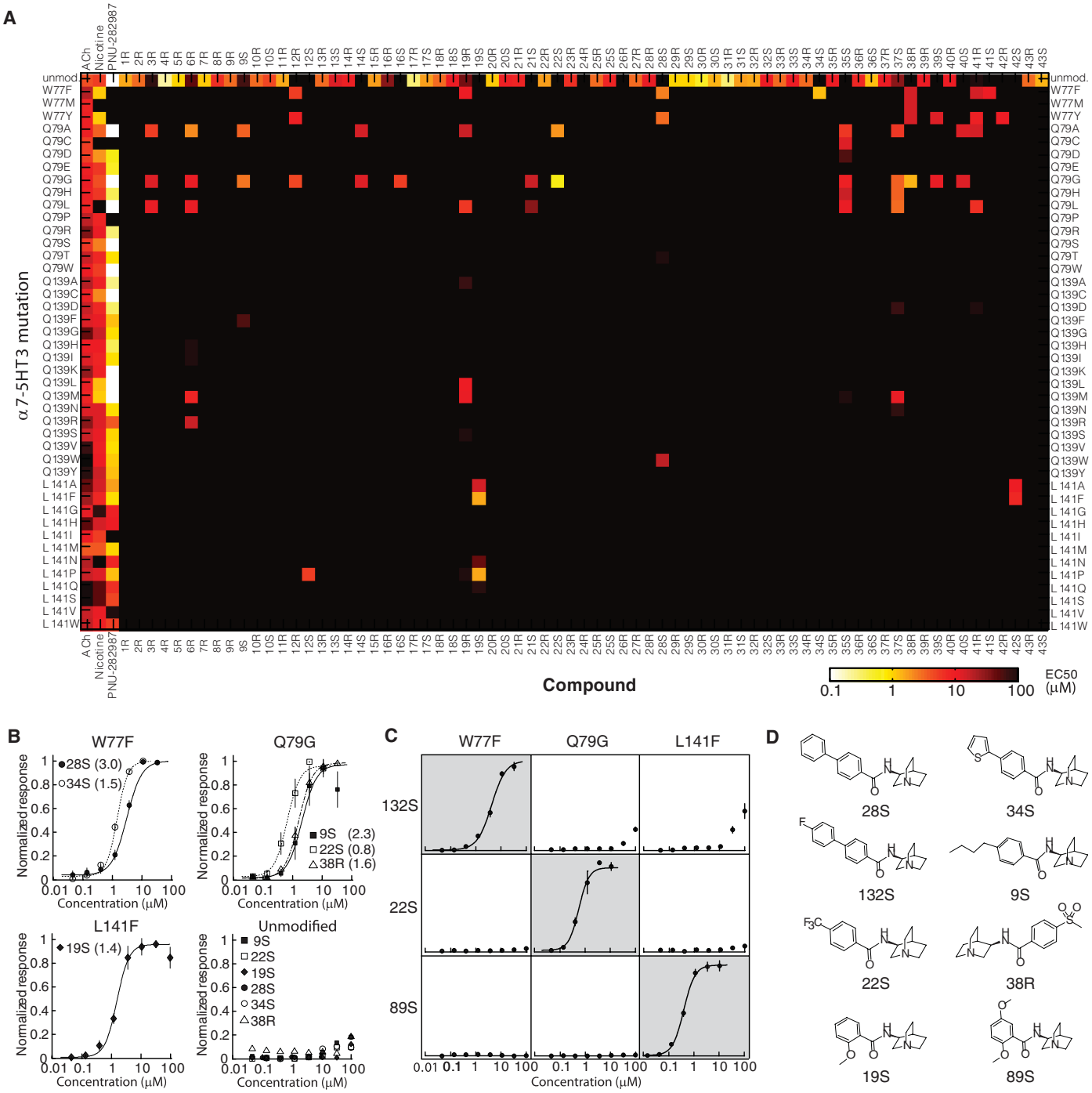

Fig. 2. Selective interactions between ligands and mutated α7-5HT3 chimeric ion channels. (**A**) Color map showing EC_{50}s for mutated α7-5HT3 with ACh, nicotine, and aminoquinuclidine benzamides. To highlight molecules that are highly selective for mutated α7-5HT3 chimeric receptors, only the activity of molecules with EC_{50} > 30 μM against unmodified α7-5HT3 (top row) is shown for the mutated receptors. (**B**) Dose response curves for compounds with mutated channels, showing negligible activation of unmodified α7-5HT3. EC_{50} values from the MP assay are shown in parentheses. Normalization is to the maximum response to each compound or to ACh (for unmodified α7-5HT3). (**C**) Dose response curves for mutated ion channel–ligand interactions that show orthogonal pharmacology. Normalization is to maximum response for each compound across mutated channels. Error bars in (B) and (C) are SEM. (**D**) Chemical structures of ligands in (B) and (C).

current (I_{ss}), where I_{ss}/I_{peak} = 0.09 ± 0.07 (Fig. 1D). Because we aimed to activate conductances for minutes, we used I_{ss} to assess ligand potency. Dose responses from a fluorescence plate reader–compatible membrane potential (MP) assay reflected I_{ss} resulting from sustained ligand activation of the channel (Fig. 1D and table S1). Mutations at Gln^{79}, Gln^{139}, and Leu^{141} were tolerated functionally, whereas for Trp^{77} only Tyr, Phe, and Met mutations produced ACh-responsive channels (Fig. 1E). In total, 43 mutated ion channels were selected for additional dose response assays.

We synthesized a focused chemical library of 71 enantiomerically pure 3-aminoquinuclidine benzamide candidate ligands to test against mutated α7-5HT3 channels (fig. S2). Because benzamide substituents at C2 and C4 can adversely affect α7-5HT3 channel activation (*21*), our library emphasized these substitution patterns. Compounds that exhibited low activity at α7-5HT3 (Fig. 2A) were selected for further analysis.

Using the MP assay, we measured 1118 dose response curves for 43 mutated α7-5HT3 channels against 23 3-aminoquinuclidine benzamides as well as ACh, nicotine, and PNU-282987 (Fig. 2A). Three classes of mutated ion channels—Trp^{77} → Phe (W77F), Gln^{79} → Gly (Q79G), and Leu^{141} → Phe (L141F)—showed selective activity for their cognate ligands over unmodified α7-5HT3 receptor and had mean effective concentration values (EC_{50}s) of <5 μM (Fig. 2B and table S1). Channels with the W77F mutation were activated by quinuclidinyl ligands with 4-aromatic benzamide substitutions. The Q79G mutation, which likely expands the ligand-binding pocket, accommodated larger ligands such as 9S, 22S, and 38R. A third set of mutations, L141F and L141P (Leu^{141} → Pro), both showed selectivity for the 2-methoxy–substituted benzamide 19S.

To improve the selective interaction of 19S with α7-5HT3 L141F, we synthesized and tested additional alkoxybenzamide analogs (table S2). The dimethoxy derivatives, 88S and 89S, exhibited a factor of 4 to 10 improvement in potency against this mutated receptor and did not activate the unmodified α7-5HT3 receptor (tables S1 and S2).

Several ligand and ion channel combinations were also selective relative to each other (Fig. 2C). Compound 132S, a fluorinated analog of 28S (Fig. 2D), selectively activated α7-5HT3 W77F over receptors with the Q79G and L141F mutations. Similarly, 22S and 89S were orthogonally selective for Q79G and L141F, respectively. Such selectivity is critical for developing tools that allow separate manipulation of multiple ionic conductances in the same organism. These selective LBDs were used as pharmacologically selective actuator modules (PSAMs) in conjunction with their cognate pharmacologically selective effector molecule (PSEM) agonists.

To develop PSAMs for use in the brain, we also reduced responsiveness to the endogenous ligand, ACh. We focused on shifting the EC_{50} values for I_{peak} because steady-state concentrations of ACh are reported not to exceed 1 μM (*22*), which is below the activation threshold for these channels. Inspection of data in Fig. 2A revealed mutations on the complementary face of the binding pocket that diminish ACh responsiveness, which were combined with selectivity-conferring mutations to generate LBDs that retained ligand selectivity but were unresponsive to physiological levels of ACh. $PSAM^{Q79G,Q139G}$ and $PSAM^{Q79G,L141S}$ (S = Ser) were responsive to 22S and 9S, respectively, but ACh potency was reduced by a factor of 8 to 10 relative to $PSAM^{Q79G}$ (fig. S3 and table S1). For $PSAM^{L141F}$, Tyr → Phe mutation (*23*) at the ligand-binding site ($PSAM^{L141F,Y115F}$) reduced ACh responsiveness while leaving the potency of $PSEM^{89S}$ largely unaffected (table S1).

We combined PSAM, IPD, and PSEM modules to build tools for neuronal perturbations such as activation, Ca^{2+} flux, and silencing. For a robust neuron-activating cation channel, we further developed the α7-5HT3 channel by incorporating three mutations (fig. S1) reported to increase single-channel conductance (*24*). The addition of these high-conductance (HC) mutations increased membrane current noise amplitude upon PSEM application (fig. S4), consistent with higher conductance properties (*25*).

The chimeric channels were tested in brain slices as neuronal activation tools for layer 2/3 cortical neurons. These channels distributed to somatodendritic compartments (Fig. 3A). The membrane properties of neurons expressing these channels were not significantly different from those of control neurons lacking them (fig. S5). Under conditions that block neuron and network activity [tetrodotoxin and 6-cyano-7-nitroquinoxaline-2,3-dione (CNQX)], these channels depolarized

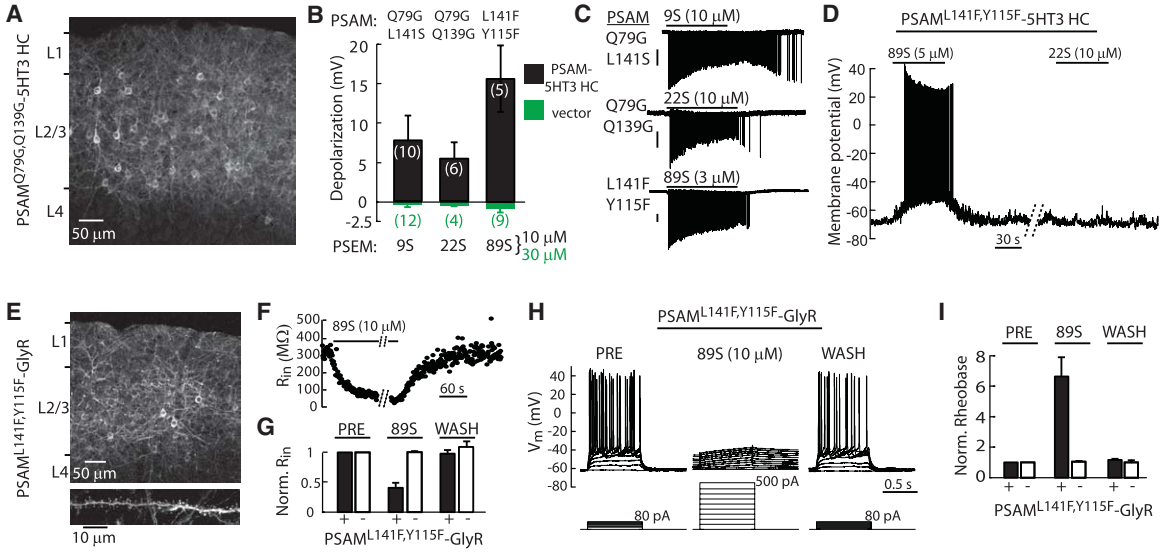

Fig. 3. PSAM-IPD chimeric ion channels for neuron activation and silencing. (**A**) Confocal projection image of α-Bgt–Alexa594 labeling in a cortical brain slice expressing $PSAM^{Q79G,Q139G}$-5HT3 HC receptors. Laminar boundaries are indicated at the left. (**B**) Depolarization of layer 2/3 cortical neurons (in tetrodotoxin and CNQX) via PSAM-5HT3 HC channels by PSEMs applied at 10 μM. PSEM application (30 μM) to control neurons electroporated with vector expressing green fluorescent protein did not depolarize cells. Sample sizes are in parentheses. (**C**) Cell-attached recordings of PSAM-5HT3 HC channel activation of layer 2/3 cortical neurons. Scale bars, 50 pA; ligand application, 120 s. (**D**) Ligand selectivity. Layer 2/3 cortical neurons expressing $PSAM^{L141F,Y115F}$-5HT3 HC are activated by $PSEM^{89S}$ but not by $PSEM^{22S}$. (**E**) Top: Confocal projection image of α-Bgt labeling in a cortical brain slice expressing $PSAM^{L141F,Y115F}$-GlyR receptors. Bottom: Dendritic segment. (**F** and **G**) $PSAM^{L141F,Y115F}$-GlyR and $PSEM^{89S}$ (10 μM, n = 16), but not $PSEM^{89S}$ alone (30 μM, n = 10), reversibly reduce cellular input resistance, R_{in}. Shown in (G) is R_{in} normalized to pre-$PSEM^{89S}$ application (PRE); values are displayed for $PSEM^{89S}$ application and after 3-min washout (WASH). (**H**) $PSAM^{L141F,Y115F}$-GlyR reversibly reduces excitability of cortical neurons to depolarizing current injection in the presence of $PSEM^{89S}$. (**I**) Rheobase, normalized to pre-$PSEM^{89S}$ application. Error bars are SEM.

neurons in the presence of the cognate PSEMs (Fig. 3B). PSEMs showed negligible effects on membrane potential in neurons lacking the channels (Fig. 3B).

We used cell-attached recordings, which do not perturb neuronal composition, to show that neurons expressing different PSAM-5HT3 HC channels sustainably increased their firing rate during PSEM application (Fig. 3C). Thus, several PSAM-5HT3 HC channels and their ligands are effective neuronal activators. The selectivity of PSEM-PSAM interactions was evident from activation of PSAM^{L141F,Y115F}-5HT3 HC by PSEM^{89S} but not by PSEM^{22S} (Fig. 3D and fig. S6). Moreover, these PSEMs did not displace radioligand binding in a panel of 23 mammalian ion channels, G protein–coupled receptors, and transporters (table S3). PSEM^{89S} and PSEM^{22S} also showed good brain penetrance in mice after minimally invasive intraperitoneal administration (fig. S7).

PSAMs can also be applied to generate pharmacologically selective ligand-gated Ca^{2+} channels. We combined PSAM^{Q79G,L141S} with the α7-nAChR IPD, a high-conductance, primarily Ca^{2+}-selective channel (*26*). Because α7 nAChR desensitizes rapidly, we tested channel pore mutations reported to reduce the desensitization properties of these channels. We found that α7 nAChR Q79G L141S modified with the channel pore mutation V13′T (*27*) (here V274T; fig. S8) was nondesensitizing in response to PSEM^{9S}, showing sustained activation and Ca^{2+} influx (fig. S9 and movie S1). Such channels are potentially useful for inducing Ca^{2+}-dependent processes in specific cell populations.

To construct neuron-silencing tools, we generated chimeric channels with the use of PSAM^{Q79G} or PSAM^{L141F} fused to the glycine receptor (GlyR) chloride-selective IPD (*12*) (fig. S10). A similar channel was constructed using PSAM^{L141F} fused to the γ-aminobutyric acid type C ($GABA_C$) receptor IPD (fig. S11), illustrating the relative ease of generating new chimeric channels by combinations of PSAMs with IPDs. These channels exhibited a slow time course for activation (fig. S12) and low ACh potency (table S1); both properties have been described previously for α7-GlyR (*12*). ACh responsiveness was further diminished by modifying PSAM^{L141F}-GlyR with the Y115F mutation (table S1).

Expression of PSAM^{L141F,Y115F}-GlyR in layer 2/3 cortical neurons showed somatodendritic distribution (Fig. 3E) and was well tolerated (fig. S5). PSEM^{89S} (10 μM) reversibly silenced transfected neurons by reducing cellular input resistance (Fig. 3, F and G). This shunt contributed to a reversible increase by nearly a factor of 7 in the magnitude of injected current required to fire an action potential (rheobase) (Fig. 3, H and I), and some cells did not fire even with 500 pA of injected current. In contrast, vector-transfected control neurons (n = 11) were unaffected by a higher concentration of PSEM^{89S} (30 μM; Fig. 3, G and I). Thus, PSAM^{L141F,Y115F}-GlyR and PSEM^{89S} constitute a powerful neuronal silencing system. Furthermore, the pharmacology of this neuron-silencing system is orthogonal to the PSAM^{Q79G,Q139G}-5HT3 HC–PSEM^{22S} neuronal activator system (figs. S6 and S13), indicating the feasibility of using these tools in concert.

To test the effectiveness of a PSEM–PSAM-IPD system in vivo, we examined the capacity of a neuronal silencer to influence behavior in mice. We used PSAM^{L141F,Y115F}-GlyR and PSEM^{89S} in hypothalamic *Agouti-related protein*–expressing (AGRP) neurons to suppress voracious eating evoked by photostimulation of these neurons coexpressing the light-activated cation channel, channelrhodopsin-2 (ChR2) (*8*, *9*). The stringency of this behavioral assay as a test for a neuronal silencer tool is due to the strong synchronous input from ChR2 activation. Moreover, because the magnitude of AGRP neuron–evoked food

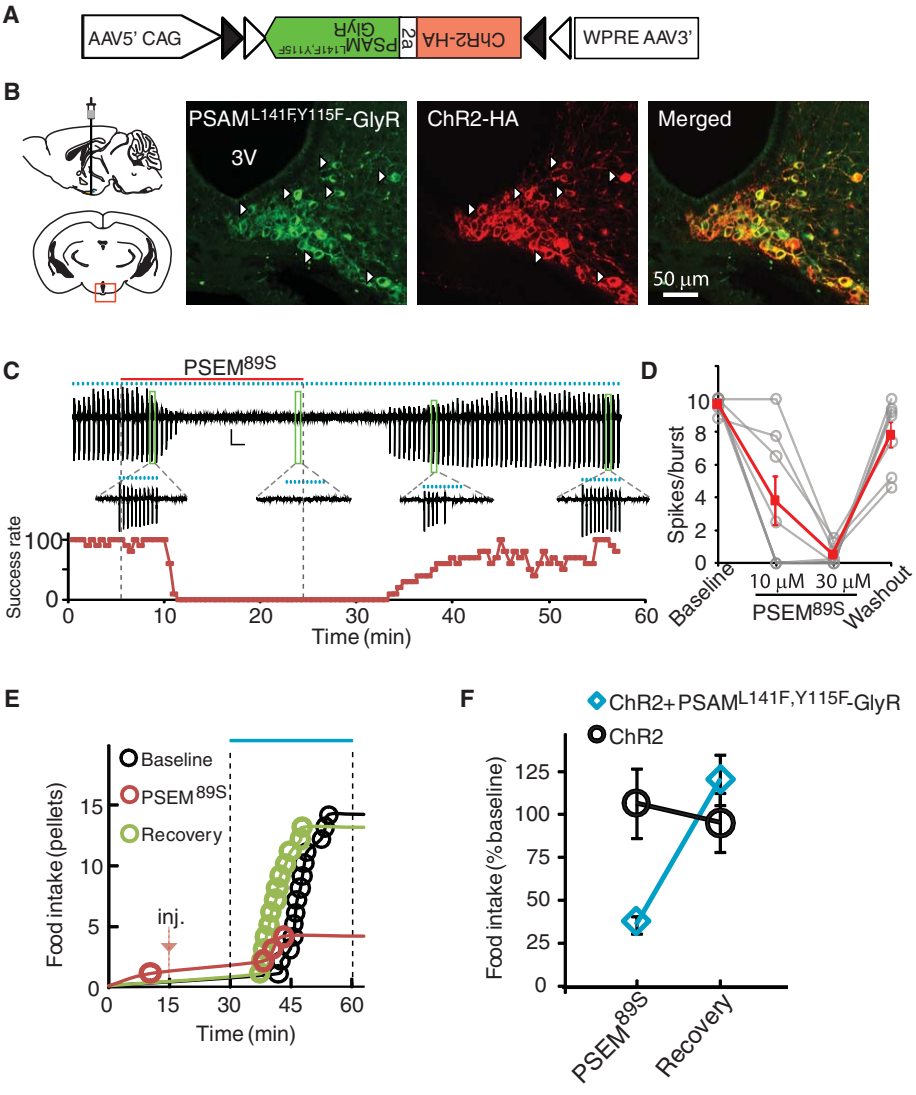

Fig. 4. Stringent neuronal silencing test of PSAM^{L141F,Y115F}-GlyR for suppressing AGRP neuron-evoked feeding behavior. (**A**) Construct for a Cre-dependent recombinant adeno-associated viral vector with an inverted bicistronic open reading frame for PSAM^{L141F,Y115F}-GlyR and ChR2 under control of a FLEX-switch [two antiparallel pairs of heterotypic loxP sites (triangles)]. (**B**) Diagram illustrating injection site (left) and confocal images (right) taken from brain slices of virally transduced *Agrp-cre* mice showing coexpression of PSAM^{L141F,Y115F}-GlyR (green, α-Bgt–Alexa488) and ChR2 (red, antibody to hemagglutinin). (**C**) Cell-attached recording showing suppression of light-evoked bursts of action potential currents (10-Hz light pulses for 1 s, represented by blue dots) after application and then washout of PSEM^{89S} (above). Bursts are expanded for selected time points. Below is spike success rate (percent) before, during, and after PSEM^{89S} application. (**D**) Successful light-evoked spikes per burst (n = 8 cells). (**E**) Food intake on successive days resulting from photostimulation in an *Agrp-cre* mouse coexpressing ChR2 and PSAM^{L141F,Y115F}-GlyR after saline (baseline and recovery) or PSEM^{89S} [intraperitoneal injection (inj.), marked with red arrow]. (**F**) Evoked food intake normalized to initial photostimulation session. Injection of PSEM^{89S} reduced photostimulation-evoked eating in *Agrp-cre* mice coexpressing ChR2 and PSAM^{L141F,Y115F}-GlyR (30 mg/kg, blue diamonds, n = 5 mice) but not in *Agrp-cre* mice expressing only ChR2 (50 mg/kg, black circles, n = 6 mice). Error bars are SEM.

consumption varies continuously with the level of AGRP neuron activation, nearly full suppression of activity is required to block the evoked feeding response (*28*).

AGRP neurons in *Agrp-cre* mice (*29*) were transduced using a bicistronic Cre recombinase (Cre)–dependent viral vector (*30*) (Fig. 4A). AGRP neurons coexpressing ChR2 and PSAM^{L141F,Y115F}-GlyR (Fig. 4B) could be activated with light and were reversibly silenced by PSEM^{89S} during photostimulation in brain slices (Fig. 4, C and D). Mice coexpressing ChR2 and PSAM^{L141F,Y115F}-GlyR or expressing ChR2 alone in AGRP neurons ate voraciously in response to photostimulation after intraperitoneal (i.p.) saline injection, and, for each mouse, this consumption was used as the baseline for subsequent treatments. After i.p. administration of PSEM^{89S}, photostimulation-evoked feeding was strongly suppressed in mice expressing PSAM^{L141F,Y115F}-GlyR but not in mice expressing only ChR2 (Fig. 4, E and F). Twenty-four hours later, photostimulation-evoked food intake recovered to baseline levels (two-way analysis of variance, one-factor repeated measure, ±PSEM^{89S}: $F_{1,9} = 12.9$, $P = 0.006$; ±PSAM^{L141F,Y115F}-GlyR: $F_{1,9} = 1.3$, $P = 0.30$; interaction: $F_{1,9} = 22.4$, $P < 0.001$; Fig. 4, E and F). Moreover, after photostimulation, Fos, a marker of neuron activation (*31*), was almost completely suppressed in ChR2-expressing neurons from mice administered PSEM^{89S} (fig. S14). Thus, PSAM^{L141F,Y115F}-GlyR and PSEM^{89S} constitute an effective neuronal silencer system in vivo, even for strong, synchronous depolarizing currents that result from ChR2 photoactivation.

Our results show how concerted chemical and genetic engineering of a complex ligand-binding interface can be used to develop pharmacologically selective actuators and small-molecule effectors for construction of a LGIC toolbox. PSEMs, the agonists for the resulting ion channels, act rapidly in the brain after peripheral delivery. Together, these components enable combinatorial construction (fig. S15) of cell type–selective tools to control a range of conductances, which can be used to activate or silence neurons. These ion channels could be further elaborated by applying extensive structure-function relationships in Cys-loop receptors, including mutations that modify ion selectivity (*27*, *32*–*34*), intracellular interactions (*35*–*37*), and desensitization (*27*, *38*, *39*). The pharmacologically orthogonal ion channels described here can also be used with each other or with existing tools such as channelrhodopsin, facilitating multiple perturbations in the same organism to investigate functions of ion flux in cell biology, physiology, and behavior.

References and Notes

1. E. M. Slimko, S. McKinney, D. J. Anderson, N. Davidson, H. A. Lester, *J. Neurosci.* **22**, 7373 (2002).
2. E. M. Tan *et al.*, *Neuron* **51**, 157 (2006).
3. P. Wulff *et al.*, *Nat. Neurosci.* **10**, 923 (2007).
4. B. N. Armbruster, X. Li, M. H. Pausch, S. Herlitze, B. L. Roth, *Proc. Natl. Acad. Sci. U.S.A.* **104**, 5163 (2007).
5. S. Gosgnach *et al.*, *Nature* **440**, 215 (2006).
6. W. Lerchner *et al.*, *Neuron* **54**, 35 (2007).
7. S. M. Ferguson *et al.*, *Nat. Neurosci.* **14**, 22 (2011).
8. E. S. Boyden, F. Zhang, E. Bamberg, G. Nagel, K. Deisseroth, *Nat. Neurosci.* **8**, 1263 (2005).
9. X. Li *et al.*, *Proc. Natl. Acad. Sci. U.S.A.* **102**, 17816 (2005).
10. F. Zhang *et al.*, *Nature* **446**, 633 (2007).
11. J. L. Eiselé *et al.*, *Nature* **366**, 479 (1993).
12. T. Grutter *et al.*, *Proc. Natl. Acad. Sci. U.S.A.* **102**, 18207 (2005).
13. H. A. Lester, M. I. Dibas, D. S. Dahan, J. F. Leite, D. A. Dougherty, *Trends Neurosci.* **27**, 329 (2004).
14. J. A. Dent, *J. Mol. Evol.* **62**, 523 (2006).
15. A. Tasneem, L. M. Iyer, E. Jakobsson, L. Aravind, *Genome Biol.* **6**, R4 (2005).
16. Y. W. Hwang, D. L. Miller, *J. Biol. Chem.* **262**, 13081 (1987).
17. A. C. Bishop *et al.*, *Nature* **407**, 395 (2000).
18. Q. Lin, F. Jiang, P. G. Schultz, N. S. Gray, *J. Am. Chem. Soc.* **123**, 11608 (2001).
19. P. H. Celie *et al.*, *Neuron* **41**, 907 (2004).
20. D. P. Walker *et al.*, *Bioorg. Med. Chem.* **14**, 8219 (2006).
21. A. L. Bodnar *et al.*, *J. Med. Chem.* **48**, 905 (2005).
22. P. N. Vinson, J. B. Justice Jr., *J. Neurosci. Methods* **73**, 61 (1997).
23. J. L. Galzi *et al.*, *FEBS Lett.* **294**, 198 (1991).
24. S. P. Kelley, J. I. Dunlop, E. F. Kirkness, J. J. Lambert, J. A. Peters, *Nature* **424**, 321 (2003).
25. D. Rayes, G. Spitzmaul, S. M. Sine, C. Bouzat, *Mol. Pharmacol.* **68**, 1475 (2005).
26. P. Séguéla, J. Wadiche, K. Dineley-Miller, J. A. Dani, J. W. Patrick, *J. Neurosci.* **13**, 596 (1993).
27. J. L. Galzi *et al.*, *Nature* **359**, 500 (1992).
28. Y. Aponte, D. Atasoy, S. M. Sternson, *Nat. Neurosci.* **14**, 351 (2011).
29. C. B. Kaelin, A. W. Xu, X. Y. Lu, G. S. Barsh, *Endocrinology* **145**, 5798 (2004).
30. D. Atasoy, Y. Aponte, H. H. Su, S. M. Sternson, *J. Neurosci.* **28**, 7025 (2008).
31. J. I. Morgan, T. Curran, *Annu. Rev. Neurosci.* **14**, 421 (1991).
32. D. Bertrand, J. L. Galzi, A. Devillers-Thiéry, S. Bertrand, J. P. Changeux, *Proc. Natl. Acad. Sci. U.S.A.* **90**, 6971 (1993).
33. A. Keramidas, A. J. Moorhouse, C. R. French, P. R. Schofield, P. H. Barry, *Biophys. J.* **79**, 247 (2000).
34. M. J. Gunthorpe, S. C. Lummis, *J. Biol. Chem.* **276**, 10977 (2001).
35. M. K. Temburni, R. C. Blitzblau, M. H. Jacob, *J. Physiol.* **525**, 21 (2000).
36. J. Xu, Y. Zhu, S. F. Heinemann, *J. Neurosci.* **26**, 9780 (2006).
37. M. Jansen, M. Bali, M. H. Akabas, *J. Gen. Physiol.* **131**, 137 (2008).
38. F. Revah *et al.*, *Nature* **353**, 846 (1991).
39. H. G. Breitinger, C. Villmann, K. Becker, C. M. Becker, *J. Biol. Chem.* **276**, 29657 (2001).

Acknowledgments: Supported by the Howard Hughes Medical Institute. C.J.M. performed the electrophysiology and the imaging; P.H.L. synthesized the molecules and performed the MP screen; D.A. performed the behavioral experiments; H.H.S. made the mutant channels and other constructs; L.L.L. made the homology model; and S.M.S. developed the mutant ion channel screen, planned the experiments, analyzed data, and wrote the paper with comments from all authors. We thank S. Winfrey and H. White for cell culture support. S.M.S., P.H.L., and L.L.L. are inventors on a patent application by the Howard Hughes Medical Institute regarding combined use of these ligand-gated ion channels and small-molecule agonists.

Supporting Online Material

www.sciencemag.org/cgi/content/full/333/6047/1292/DC1
Materials and Methods
Figs. S1 to S15
Tables S1 to S3
Movie S1
References (*40*–*42*)

6 April 2011; accepted 8 August 2011
10.1126/science.1206606

Potential for Chemolithoautotrophy Among Ubiquitous Bacteria Lineages in the Dark Ocean

Brandon K. Swan,[1] Manuel Martinez-Garcia,[1] Christina M. Preston,[2] Alexander Sczyrba,[3] Tanja Woyke,[3] Dominique Lamy,[4]* Thomas Reinthaler,[4] Nicole J. Poulton,[1] E. Dashiell P. Masland,[1] Monica Lluesma Gomez,[1] Michael E. Sieracki,[1] Edward F. DeLong,[5] Gerhard J. Herndl,[4] Ramunas Stepanauskas[1]†

Recent studies suggest that unidentified prokaryotes fix inorganic carbon at globally significant rates in the immense dark ocean. Using single-cell sorting and whole-genome amplification of prokaryotes from two subtropical gyres, we obtained genomic DNA from 738 cells representing most cosmopolitan lineages. Multiple cells of *Deltaproteobacteria* cluster SAR324, *Gammaproteobacteria* clusters ARCTIC96BD-19 and Agg47, and some *Oceanospirillales* from the lower mesopelagic contained ribulose-1,5-bisphosphate carboxylase-oxygenase and sulfur oxidation genes. These results corroborated community DNA and RNA profiling from diverse geographic regions. The SAR324 genomes also suggested C_1 metabolism and a particle-associated life-style. Microautoradiography and fluorescence in situ hybridization confirmed bicarbonate uptake and particle association of SAR324 cells. Our study suggests potential chemolithoautotrophy in several uncultured *Proteobacteria* lineages that are ubiquitous in the dark oxygenated ocean and provides new perspective on carbon cycling in the ocean's largest habitat.

The dark ocean (below 200 m) contains an active and metabolically diverse microbial assemblage that is responsible for the majority of marine organic carbon mineralization (*1*). In addition to heterotrophic microbial activity, autotrophic carbon assimilation may be significant not only in oxygen minimum zones (OMZs) and anoxic basins (*2*–*4*), but also